

pubs.acs.org/journal/apchd5 Letter

GaN Magic Angle Laser in a Merged Moiré Photonic Crystal

Alexander Raun,* Haoning Tang, Xueqi Ni, Eric Mazur, and Evelyn L. Hu



Cite This: ACS Photonics 2023, 10, 3001–3007



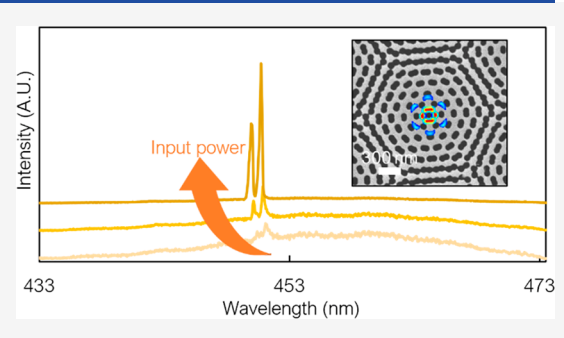
ACCESS I

Metrics & More

Article Recommendations

Supporting Information

ABSTRACT: We demonstrate optically pumped blue lasing at room temperature in a merged moiré photonic crystal fabricated out of gallium nitride with embedded, fragmented quantum wells. Lasing occurs at two closely spaced wavelengths of 450 and 451 nm, matched to simulated flat bands induced by the moiré superlattice. Both thresholds occur at $30~\mu\text{J/cm}^2$. Light in–light out curves were taken at both room temperature and 77 K across different gain materials, including fragmented quantum wells, continuous quantum wells, and quantum dots. Lasing was observed only at room temperature in fragmented quantum well devices, suggesting the importance of gain material carrier dynamics in unconventional laser cavities like the moiré design explored. These insights and the experimental



validation of moiré simulations in a previously unexplored III-V material indicate promise toward a new kind of efficient, tunable laser.

KEYWORDS: gallium nitride, blue lasing, twisted photonic structures, quantum wells, flat band

INTRODUCTION

Moiré photonic crystals, inspired by moiré electronic systems like twisted bilayer graphene, have recently garnered attention for their potential as novel, light-confining structures.⁶⁻¹³ Consisting of two stacked photonic crystals separated by a subwavelength interlayer separation distance, moiré photonic crystal systems achieve flat photonic bands when the two photonic crystal layers are twisted at a so-called "magic" angle with respect to each other. As shown in Figure 1a, the bilayer moiré system can also be collapsed into a single photonic crystal layer, which we refer to as a "merged" moiré structure. The flat photonic bands in these moiré systems slow light propagation in highly localized regions of the moiré superlattice, forming cavity-like modes. Simulations suggest these flat band modes can achieve optimal combinations of high-Q values and small mode volumes when compared to more traditional photonic crystal cavities.⁶ Beyond these advantages, the twist angle, separation thickness, and layer thicknesses as design parameters present opportunities to actively tune both the wavelength and the spatial distribution of the modes, a capability that is advantageous for many applications, including quantum photonics/light sources 14,15 and on-chip photonic signal processing. 16,17

These exciting properties of moiré photonic crystals have sparked a specific interest in using them as a new kind of low threshold, microscale laser. While there is a growing body of simulation work being carried out on moiré photonic crystal systems, experimental realizations of moiré photonic crystal lasers have yet to be thoroughly studied in a variety of wavelength regimes and incorporating different gain material types. Gallium nitride (GaN), a previously unexplored material

for a moiré lasing study, is an exciting candidate as it emits light efficiently in the visible regime at room temperature and is well-established in solid state lighting. We had previously observed ultralow threshold lasing in GaN-based microcavities such as microdisks, microrings, and nanobeams with indium gallium nitride (InGaN) quantum wells (QWs), "fragmented" quantum wells (fQWs), and quantum dots (QDs)^{19–21} (see ref 20 for a more detailed description of fQWs). Key to these devices' strong performance is an optimal overlap between the emitting material and cavity modes, both spectrally and spatially. Carrier capture and confinement properties of the gain material are also critical parameters in the lasing process, and our previous studies have probed these dynamics to understand their contributions to lasing in traditional cavity geometries.

This paper extends our knowledge of that gain material to a merged moiré photonic crystal cavity. Utilizing InGaN fQW, QW, and QD active areas, moiré cavity modes are demonstrated in all samples, but optically pumped lasing is observed only for the cavities embedded with InGaN fQWs at room temperature. Our results reveal two lasing modes closely spaced together (separated by ~ 1 nm) that correspond closely to predictions given by simulations. We observe lasing in these modes, upon pumping at a threshold optical power of 30 μ J/

Received: July 26, 2023 Published: September 8, 2023





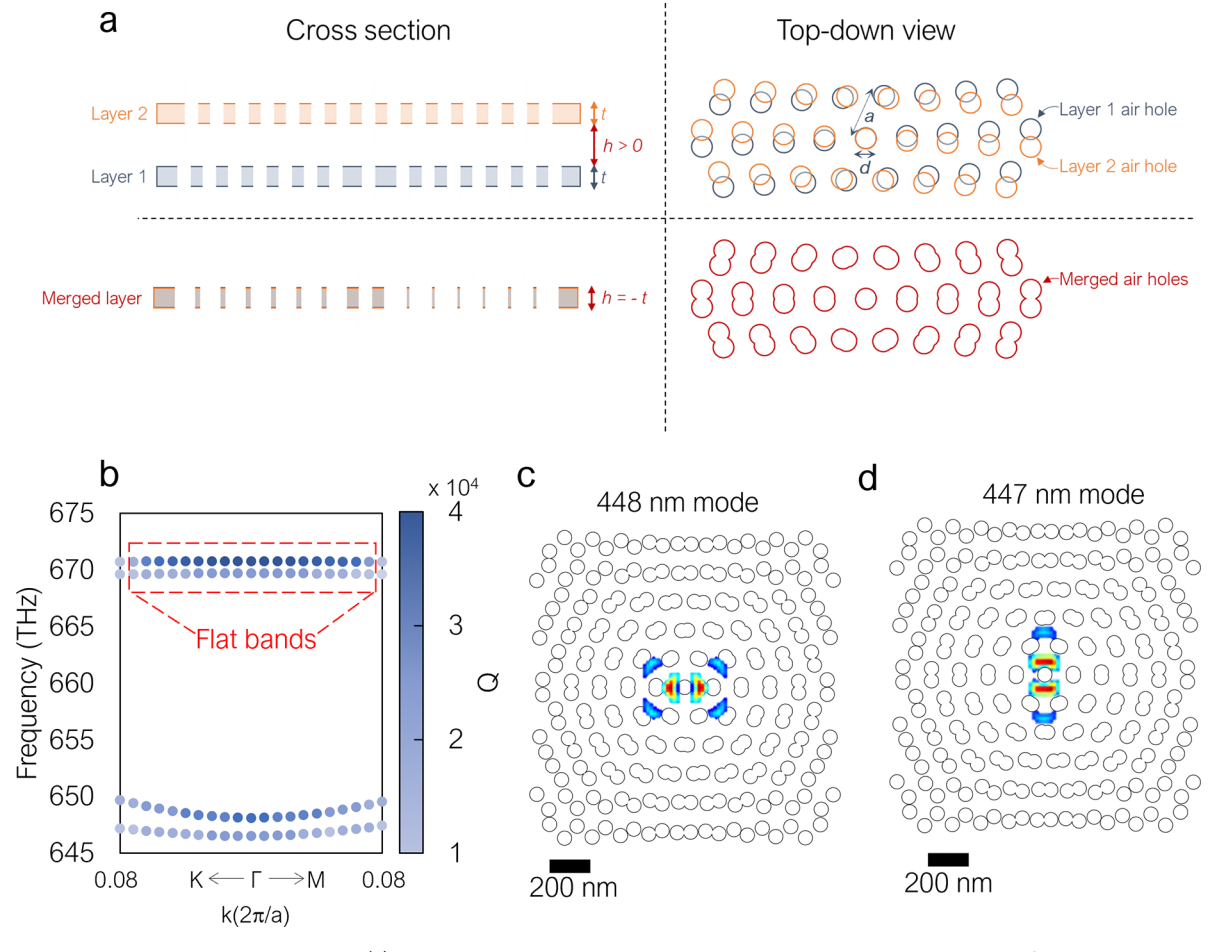


Figure 1. System schematic and simulations. (a) Schematic showing side and top-down views of a true bilayer moiré system and a single layer merged moiré system: t = thickness of each photonic crystal layer, h = interlayer distance in air between the two layers, d = air hole diameter for a single triangular lattice layer, a = lattice constant for a single triangular lattice layer; (b) Simulated band structure highlighting flat band modes for a merged, 6° twist angle. This graph is expanded in the k-region most closely surrounding the Gamma point of the Brillouin zone (c); (d) 6° twist angle design corresponding to simulation results in (b); The single layer pattern of holes in each individual layer is a triangular lattice with an air hole with a diameter d = 80 nm and a lattice constant a = 165 nm. Overlaid on the design is the mode profile, $|H_z|^2$, with the 447 nm mode shown in (c) and the 448 nm mode shown in (d).

cm². These results are encouraging for the realization of moiré photonic crystal lasers in the visible regime.

EXPERIMENTAL METHODS

Materials and Simulations. We use GaN-on-sapphire samples with up to 5 layers of embedded InGaN emitters, grown by collaborators from the Oliver group at the University of Cambridge. The GaN membrane containing the InGaN gain material is 200 nm thick and can be suspended through the removal of a 200 nm thick sacrificial super lattice (SSL) grown directly below (wafer stack schematic is shown in Figure S1). We choose to focus only on a merged single layer moiré lattice in this initial study because of several fabrication advantages. First, the fabrication of a single suspended photonic crystal is simpler than precisely aligning two photonic crystals on top of each other with a defined spacer material thickness in between. Second, by merging the two layers, we ensure that the wave functions of propagating waves in each layer enjoy maximal overlap, ultimately allowing for larger magic twist angles to be realized.²² On top of providing more design options for realizing an effective laser cavity, higher twist angle patterns are easier from a fabrication perspective, as the unit cells are smaller (requiring a smaller overall structure with less

periodicity), and there are smaller regions of continuously merged air holes, leading to less probability of membrane collapse. While the merged design results in lower theoretical Q factors, as the flat bands have greater probability of coupling to nonlocalized Bloch modes present in each individual lattice, and is fixed (removing any possibility of active tuning or twisting), the fabrication simplicity of a single layer proved most useful for an initial study.

Band diagram simulations were performed in COMSOL Multiphysics 5.6 and validated in Lumerical. To determine the ideal geometry of a merged, single layer moiré photonic crystal, we simulated a 200 nm thick GaN (n = 2.5) layer with embedded dipole sources corresponding to our InGaN emitters, emitting in the range of 430–470 nm. As shown in Figure 1a, in a merged pattern, the interlayer thickness of air, h, = -t, or in this case, -200 nm. This results in a superimposed moiré pattern written into a single slab of GaN with embedded InGaN gain material. Further details on the simulation approach can be found in ref 7.

Fabrication. Electron beam lithography was used to form a mask containing the merged moiré pattern in a negative resist, hydrogen silsesquioxane (HSQ). Unlike traditional photonic crystal cavities, a merged moiré pattern has a unit cell structure

with much more dielectric in the center of the unit cell regions than at the edges of the unit cell regions. This requires careful, optimized proximity effect correction in the electron beam lithography to ensure proper exposure in all regions of the moiré pattern.

After lithographic patterning, a chlorine-based reactive ion etch (RIE) is performed to etch the GaN vertically through the patterned mask, transferring the moiré pattern from the mask to the GaN. Due to the air holes' small size and high density, a high (~250 V) etching bias must be used to ensure steep enough sidewalls that extend all the way through the GaN membrane and into the underlying SSL (the SSL is directly below the GaN membrane and is 200 nm thick; therefore, a minimum of 400 nm must be etched in this step). Additionally, the aspect ratio of the columns to be etched (~400 nm/80 nm = 5:1) accentuates ion scattering that may lead to nonvertical sidewalls, resulting in etched features smaller than the original mask dimensions. Therefore, we deliberately created largerthan-designed feature sizes of the moiré pattern in the mask so that the etched hole sizes in the GaN would be the desired 80 nm. Upon completion of RIE etching, the HSQ mask is removed in buffered oxide etchant, and a Ti/Au metal grid is deposited on the chip surrounding each moiré lattice. This metallic contact is used in the final step of a bandgap selective photoelectrochemical etch used to remove the SSL, resulting in a suspended moiré photonic crystal slab. More details of this undercut etching can be found in Tamboli et al.²³

Optical Characterization. After fabrication, the moiré lattices were probed using an external, femtosecond pulsed 390 nm laser with a repetition rate of 76 MHz. Via a 100× objective lens, the excitation spot is estimated to be ~952 nm in diameter. The emission from the moiré structures is collected through the same objective and directed to a spectrometer. Since the moiré structures are much larger than the excitation beam spot, we scan our excitation across the entire sample to find dominant modes on which we can then take lasing data on. Moiré lattices fabricated with embedded QDs, QWs, and fQWs were all tested in our confocal photoluminescent setup, both at room temperature and at 77 K.

RESULTS AND DISCUSSION

Simulation results are presented in Figure 1b-d. We started by finding the fundamental TE mode of a single GaN photonic crystal lattice (a triangular lattice with circular air holes). This served as a basis, providing a fundamental mode (band) and bandgap. Subsequently the moiré-lattice-facilitated scattering served as coupling terms in a Hamiltonian matrix, and these may be manifested as moiré modes within the bandgap. For various twist angles in the merged design, we looked for localized flat band frequencies above the fundamental mode but within the (twist-dependent) bandgap. Through this process, the individual lattice design parameters were tuned to place the flat band modes in the desired wavelength range of the emitters; the optimal parameters included air hole diameters d = 80 nm and a lattice constant a = 165 nm. Simulation results produced band diagrams revealing flat bands across the Brillouin zone at several magic twist angles, and Figure 1b shows the flat band result for a magic twist angle of 6°, with k values immediately around the Gamma point of the Brillouin zone. This reveals two flat bands very closely spaced together in frequency, corresponding to free space wavelengths of 447 and 448 nm, which overlap with the emission region of

our InGaN emitters. The higher frequency flat band's bandwidth across the Brillouin zone is 0.48THz, and the lower frequency flat band's bandwidth is 0.45THz. The simulated Q factors of these modes are $\sim (3-4) \times 10^4$. While the Q values of these merged moiré patterns are high over the Brillouin zone and are comparable to other simulated Q's of traditional GaN photonic crystals, ²⁴ in general they are lower than for their constitutive, unmerged monolayer patterns. This is intuitively reasonable, as the increased area of holes in the merged moiré pattern presents a greater number of surface—air interfaces and therefore greater coupling of the cavity fields to the external environment (see Figure 2a,b).

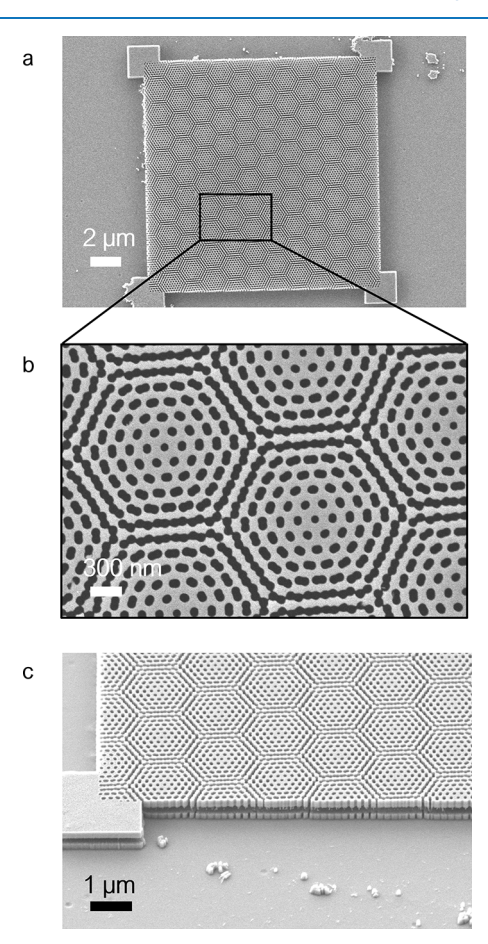


Figure 2. Scanning electron micrographs (SEMs) of fabricated moiré lattices. (a) Top-down view of the entire moiré lattice. (b) Inset zooming into portion of lattice from (a). (c) Tilted view of moiré lattice showing the undercut.

Additionally, the simulated Q of the merged moiré design is limited by the reduced thickness of the suspended slab, which is a material constraint that can lead to increased light leakage. The flat band modes from our simulations result in field localization at the center of the hexagonal unit cells in the moiré pattern (Figure 1c,d) with a mode volume of 1.07 (λ /n)³. The combination of these modes' high Q values and strongly localized mode volumes, together with their twistangle tunability, leads to the distinctive character of these cavities. The field profiles (Figure 1c,d) of these two flat bands at the Γ -point reveal two perpendicularly polarized TE-modes, which is a phenomenon realized in other moiré photonic crystal cavities ¹⁸ (polarization characterization of our devices can be found in Figure S5).

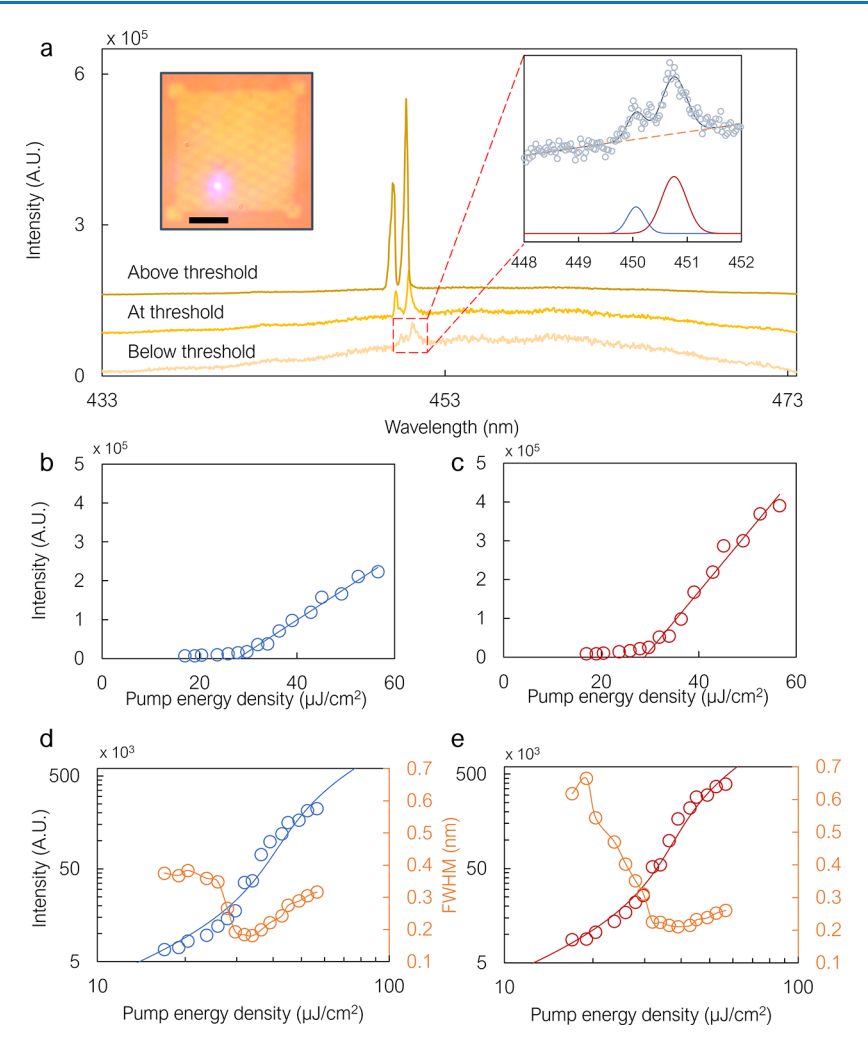


Figure 3. Optical characterization and lasing curves of the merged moiré lattice. (a) Spectra below, at, and above lasing threshold input energy. The left inset shows an optical image of the moiré sample light emission at the position where lasing was observed. Scale bar is 5 μ m. The right inset shows a zoomed in spectrum below threshold, revealing two fitted peaks, each with Q of 1175 (450 nm mode) and 829 (451 nm mode); (b, c) Linear light in–light out plots of the 450 nm, 451 nm mode (linear fits were done on the post-threshold portions to show the value of the threshold clearly on the *x*-axis) and (d, e) log–log light in–light out plots of the 450 nm, 451 nm mode; These also show the line width as a function of input power. Fits were done on these data to determine the spontaneous emission factor, β, and the cavity loss rate, γ.

While simulations revealed multiple magic twist angle designs with corresponding flat bands, we moved forward with fabrication and photoluminescent (PL) characterization of the 6° twist design due to its placement of flat bands within the bandgap and its relatively large twist angle, which provides the fabrication advantages discussed above.

Fabrication results of a merged 6° moiré lattice are presented in Figure 2, and the critical dimensions cited above (air hole diameters of 80 nm and a lattice constant a=165 nm) coupled with the pattern's high density of features reveal some of the challenges in high-quality fabrication of these cavities. The scanning electron micrographs (SEMs) in Figure 2a,b of a fabricated 6° twist angle moiré lattice show a good match between the features in the design (hole size, lattice constant) and the features in the fabricated device. The SEM also shows four square-shaped pedestals at each corner of the lattice, which are used as supports to suspend the slab. Figure 2c is a tilted view, showing the successful suspension of the lattice in air separated from the underlying substrate.

The room-temperature spectra of emitted light from a 5-layer fQW moiré lattice at increasing input powers are shown in Figure 3a. While all three samples (QD, QW, fQW) revealed

modes at room temperature near the flat band region, suggested by simulations (see Figures S2-S4), upon pumping each device at higher input powers, the only devices to consistently make the transition to lasing incorporated fQWs. The clear signature of these modal peaks in the room temperature PL, in the presence of the background emission from QDs, QWs, or fQW, is evidence of coupling of photons from the active layers to the cavity. The spectra in Figure 3a show two lasing modes at 450 and 451 nm, closely matching the two flat band modes near 450 nm, predicted from the simulations. The ability to distinguish these modes experimentally is significant, as their proximity in wavelength and spatial distribution makes them highly susceptible to hybridization. The corresponding light in-light out curves are shown in Figure 3b,c for each mode. Thresholds for both modes occur roughly at the same input energy of 30 μ J/cm². These input values have been calculated and corrected to consider reflections of the excitation at the GaN/air interface, absorption in the fQW layers, and interaction area of the crystal with the excitation beam spot (details on threshold calculation and assumptions can be found in Supporting Information). The log-log plots of these data, presented in

Figure 3d,e, show characteristic S-shaped curves associated with lasing behavior. These S-curves were fitted using the spontaneous emission factor, β , and cavity loss rate, γ , as the fitting parameters. β values of 0.87 (450 nm mode) and 0.89 (451 nm mode) and γ values of 6.34 \times 10¹¹ s⁻¹ (450 nm mode) and $4.54 \times 10^{11} \text{ s}^{-1}$ (451 nm mode) were found through these fits. R² values for each fit were 0.96 (450 nm mode) and 0.98 (451 nm mode). Constant parameters in the curve fitting for both modes included a transparency carrier density of 1×10^{27} m⁻³, a spontaneous emission lifetime of 8 ns, and an active material volume of 1.65 \times 10⁻²¹ m⁻³ (assumed to be a fraction of the mode volume determined from simulation). Finally, a vertical scaling parameter was used to account for the difference between the number of photons in the device and the number of photons detected by our spectrometer. Also plotted in Figure 3d,e are the line widths of the modes as a function of input power. Quality factors of the modes below threshold were ~1000. It is often the case that Q values for fabricated cavities can be much lower than the theoretically predicted values (in our case, $\sim (3-4) \times 10^4$) due to fabrication errors and absorption in the material. As mentioned previously, this is exacerbated in a moiré photonic crystal when compared to a traditional 2D photonic crystal, as there is a greater surface area of dielectric-air interfaces where sidewall defects (i.e., roughness) can degrade the Q. As input power is swept through the lasing threshold in our devices, we see a decrease in line width for both modes. For the 450 nm mode, the line width increases noticeably after threshold, while the 451 nm mode shows a more stable behavior postthreshold. The increase in line width for the 450 nm mode could be due to several factors, including the 451 nm mode simply dominating the lasing process, as it shows consistently higher photon output than the 450 nm mode. Additionally, this could be explained by mode hopping effects. Any mode hopping is likely to be happening on a time scale on the order of nanoseconds²⁶ and is therefore unable to be resolved by our spectrometer, which operates at an integration time of 0.1 s. Another factor could be an increase in the effective refractive index due to excess carrier generation and/or increased temperatures reached post threshold. Finally, as mentioned above, there could be hybridization happening between these modes as they are so close to each other spectrally and spatially, and any lattice imperfections like strain or asymmetry could lead to this hybridization.

The fact that lasing was only observed at room temperature with fQWs suggests the importance of carrier dynamics in the lasing process and the sensitivity of the coupling between the moiré flat bands and the emission spectrum of the gain material. While QDs theoretically provide the best carrier confinement and radiative recombination rates, their epitaxial growth is stochastic in both size and placement, meaning that there is a low likelihood of a perfectly sized QD to match spectrally with a flat band mode while also being well positioned within the small mode volume of that flat band mode. In fact, with an areal density of $\sim 1 \times 10$ cm⁻², there are only 3 QDs on average found within one of the flat band mode field maxima (shown in Figure 1c,d). QWs and fQWs do not have this issue of spatial placement in the cavity, as they are continuous or mostly continuous throughout the GaN membrane, ensuring a higher probability of overlap with the flat band mode volume. However, as QWs confine carriers in only one dimension, those carriers may readily diffuse away from the localized modal volume. Moreover, through this diffusion, such carriers can encounter traps, leading to nonradiative recombination pathways and particularly at surface states between the dielectric and air at hole edges in the photonic crystal. Overall, this inefficiency makes lasing much more challenging at high input powers. Increasing pump powers to either (1) increase carrier capture within QDs or (2) enhance radiative recombination in QWs also produces changes in the effective index of the material and is a source of disorder (i.e., heating) for the laser.

fQWs are essentially a "happy medium" between QDs and QWs, as they are large enough to ensure good overlap with the flat band modes spatially while also providing better carrier confinement and the prevention of carriers recombining at surface states in the photonic crystal. We have seen this phenomenon before in nanobeam photonic crystal cavities where fQW lasers significantly outperformed QW lasers with regard to threshold.²⁷ Ultimately, we believe this to be a possible explanation for why we only saw lasing in moiré cavities with fQWs and not QDs or QWs.

Given the possibility of "heating" of the cavity structure at high input powers, we would expect better performance, i.e., lasing, if the samples were all cooled. Interestingly, when the samples were cooled to 77 K, there was no evidence of cavity modes in the PL spectra of the QD or QW samples. For the QD sample, the substantial blueshift of the spectrum reduced the spectral overlap between the mode and the emission spectrum (Figure S4). For the QW sample, although the peak of the PL spectrum also blue-shifted and should have been in resonance with the mode that was evident in the room temperature spectrum, there is no indication of a modal peak in the 77 K spectrum (Figure S3). We speculate that, at the lower temperature, diffusion lengths of the electrons and holes increase; 28 this exacerbates the room temperature situation where either nonradiative recombination takes place at the etched sidewalls of the cavity or radiative recombination takes place far away from the localized modal volume. Finally, while the fQW sample does display a modal peak at 77 K that increases with intensity at higher pump powers, we were unable to achieve lasing at lower temperature. It may be that the increased diffusion lengths of electrons and holes also play a role in limiting the lasing at 77 K for the fQW samples. Further measurements and calculations are required to fully understand both the limitations of the QD and QW samples at room temperature as well as the behavior at 77 K. These initial results underscore the importance of understanding and optimizing the details of carrier generation, localization, and recombination relative to the cavity structure.

CONCLUSION

In conclusion, we have shown visible-wavelength lasing at room temperature in GaN moiré photonic crystals embedded with InGaN fragmented quantum wells. Both observed lasing modes lase at $30~\mu J/cm^2$ and occur at wavelengths closely matching the simulated predictions. These results are critical experimental data points for validating and enhancing simulation efforts in moiré photonic systems. Additionally, our photoluminescent studies across fQWs, QWs, and QDs at different temperatures begin to elucidate the necessary carrier confinement and gain spectral characteristics for an effective moiré laser. Finally, the ability to see lasing in a GaN-based moiré device is particularly promising in validating the robustness of moiré photonic crystal lasers, as GaN devices require smaller features and have a host of inherent fabrication

difficulties. These results could open pathways to the fabrication of more complicated moiré devices, such as true bilayer systems, and additional applications where a highly tunable and sensitive cavity is needed. Overall, our lasing results in these merged moiré lattice lasers show promise for a new kind of high-quality cavity operating in the visible wavelength regime and beyond.

ASSOCIATED CONTENT

Supporting Information

The Supporting Information is available free of charge at https://pubs.acs.org/doi/10.1021/acsphotonics.3c01064.

Materials information, temperature measurements, and polarization measurements (PDF)

AUTHOR INFORMATION

Corresponding Author

Alexander Raun — School of Engineering and Applied Sciences, Harvard University, Cambridge, Massachusetts 02138, United States; orcid.org/0000-0001-8832-4197; Email: raun@g.harvard.edu

Authors

Xueqi Ni — School of Engineering and Applied Sciences, Harvard University, Cambridge, Massachusetts 02138, United States

Eric Mazur — School of Engineering and Applied Sciences, Harvard University, Cambridge, Massachusetts 02138, United States; © orcid.org/0000-0003-3194-9836

Evelyn L. Hu — School of Engineering and Applied Sciences, Harvard University, Cambridge, Massachusetts 02138, United States

Complete contact information is available at: https://pubs.acs.org/10.1021/acsphotonics.3c01064

Funding

NSF ECCS-1541959, NSF DMR-1231319, NSF ECCS-2234513, and DARPA URFAO: GR510802

Notes

The authors declare no competing financial interest.

ACKNOWLEDGMENTS

All fabrication work was done at the Harvard Center for Nanoscale Systems (CNS). The authors gratefully acknowledge Rachel Oliver's group at the University of Cambridge for growing all GaN/InGaN wafers used in this paper.

■ REFERENCES

- (1) Cao, Y.; Fatemi, V.; Fang, S.; Watanabe, K.; Taniguchi, T.; Kaxiras, E.; Jarillo-Herrero, P. Unconventional Superconductivity in Magic-Angle Graphene Superlattices. *Nature* **2018**, *556* (7699), 43–50.
- (2) Tarnopolsky, G.; Kruchkov, A. J.; Vishwanath, A. Origin of Magic Angles in Twisted Bilayer Graphene. *Phys. Rev. Lett.* **2019**, 122 (10), 106405.
- (3) Du, L.; Molas, M. R.; Huang, Z.; Zhang, G.; Wang, F.; Sun, Z. Moiré Photonics and Optoelectronics. *Science* **2023**, *379* (6639), eadg0014.
- (4) Mak, K. F.; Shan, J. Semiconductor Moiré Materials. *Nat. Nanotechnol.* **2022**, *17* (7), 686–695.

- (5) Andrei, E. Y.; Efetov, D. K.; Jarillo-Herrero, P.; MacDonald, A. H.; Mak, K. F.; Senthil, T.; Tutuc, E.; Yazdani, A.; Young, A. F. The Marvels of Moiré Materials. *Nat. Rev. Mater.* **2021**, *6* (3), 201–206.
- (6) Tang, H.; Ni, X.; Du, F.; Srikrishna, V.; Mazur, E. On-Chip Light Trapping in Bilayer Moiré Photonic Crystal Slabs. *Appl. Phys. Lett.* **2022**, *121* (23), 231702.
- (7) Tang, H.; Du, F.; Carr, S.; DeVault, C.; Mello, O.; Mazur, E. Modeling the Optical Properties of Twisted Bilayer Photonic Crystals. *Light Sci. Appl.* **2021**, *10* (1), 1–8.
- (8) Tang, H.; Lou, B.; Du, F.; Zhang, M.; Ni, X.; Xu, W.; Jin, R.; Fan, S.; Mazur, E. Experimental Probe of Twist Angle—Dependent Band Structure of on-Chip Optical Bilayer Photonic Crystal. *Sci. Adv.* **2023**, *9* (28), eadh8498.
- (9) Nguyen, D. X.; Letartre, X.; Drouard, E.; Viktorovitch, P.; Nguyen, H. C.; Nguyen, H. S. Magic Configurations in Moiré Superlattice of Bilayer Photonic Crystals: Almost-Perfect Flat bands and Unconventional Localization. *Phys. Rev. Res.* **2022**, *4* (3), L032031.
- (10) Oudich, M.; Su, G.; Deng, Y.; Benalcazar, W.; Huang, R.; Gerard, N. J. R. K.; Lu, M.; Zhan, P.; Jing, Y. Photonic Analog of Bilayer Graphene. *Phys. Rev. B* **2021**, *103* (21), 214311.
- (11) Alnasser, K.; Kamau, S.; Hurley, N.; Cui, J.; Lin, Y. Photonic Band Gaps and Resonance Modes in 2D Twisted Moiré Photonic Crystal. *Photonics* **2021**, *8* (10), 408.
- (12) Wang, P.; Zheng, Y.; Chen, X.; Huang, C.; Kartashov, Y. V.; Torner, L.; Konotop, V. V.; Ye, F. Localization and Delocalization of Light in Photonic Moiré Lattices. *Nature* **2020**, *577* (7788), 42–46.
- (13) Lou, B.; Fan, S. Tunable Frequency Filter Based on Twisted Bilayer Photonic Crystal Slabs. *ACS Photonics* **2022**, *9* (3), 800–805. (14) Li, F.; Li, Y.; Cai, Y.; Li, P.; Tang, H.; Zhang, Y. Tunable Open-Access Microcavities for Solid-State Quantum Photonics and Polaritonics. *Adv. Quantum Technol.* **2019**, 2 (10), 1900060.
- (15) Xia, K.; Sardi, F.; Sauerzapf, C.; Kornher, T.; Becker, H.-W.; Kis, Z.; Kovacs, L.; Dertli, D.; Foglszinger, J.; Kolesov, R.; Wrachtrup, J. Tunable Microcavities Coupled to Rare-Earth Quantum Emitters. *Optica* **2022**, *9* (4), 445.
- (16) Yüce, E.; Artvin, Z.; Sahin, R.; Bek, A.; Tasgin, M. E. Actively Tunable Photonic Crystal-Based Switch via Plasmon-Analog of Index Enhancement. *Appl. Phys. Lett.* **2021**, *119* (21), 211103.
- (17) Pustai, D. M.; Sharkawy, A.; Shi, S.; Prather, D. W. Tunable Photonic Crystal Microcavities. *Appl. Opt.* **2002**, *41* (26), 5574–5579.
- (18) Mao, X. R.; Shao, Z. K.; Luan, H. Y.; Wang, S. L.; Ma, R. M. Magic-Angle Lasers in Nanostructured Moiré Superlattice. *Nat. Nanotechnol.* 2021 1610 2021, 16 (10), 1099–1105.
- (19) Wang, D.; Zhu, T.; Oliver, R. A.; Hu, E. L. Ultra-Low-Threshold InGaN/GaN Quantum Dot Micro-Ring Lasers. *Opt. Lett.* **2018**, 43 (4), 799.
- (20) Woolf, A.; Puchtler, T.; Aharonovich, I.; Zhu, T.; Niu, N.; Wang, D.; Oliver, R.; Hu, E. L. Distinctive Signature of Indium Gallium Nitride Quantum Dot Lasing in Microdisk Cavities. *Proc. Natl. Acad. Sci. U. S. A.* **2014**, *111* (39), 14042–14046.
- (21) Aharonovich, I.; Woolf, A.; Russell, K. J.; Zhu, T.; Niu, N.; Kappers, M. J.; Oliver, R. A.; Hu, E. L. Low Threshold, Room-Temperature Microdisk Lasers in the Blue Spectral Range. *Appl. Phys. Lett.* **2013**, *103* (2), 021112.
- (22) Dong, K.; Zhang, T.; Li, J.; Wang, Q.; Yang, F.; Rho, Y.; Wang, D.; Grigoropoulos, C. P.; Wu, J.; Yao, J. Flat Bands in Magic-Angle Bilayer Photonic Crystals at Small Twists. *Phys. Rev. Lett.* **2021**, *126* (22), 223601.
- (23) Tamboli, A. C.; Haberer, E. D.; Sharma, R.; Lee, K. H.; Nakamura, S.; Hu, E. L. Room-Temperature Continuous-Wave Lasing in GaNInGaN Microdisks. *Nat. Photonics* **2007**, *1* (1), 61–64. (24) Zamani, N. D. M.; Nawi, M. N.; Berhanuddin, D. D.; Majlis, B. Y.; Md Zain, A. R. Design of 2D GaN Photonic Crystal Based on Hole Displacement for L3 Cavity. *Nanomater. Nanotechnol.* **2020**, *10*,
- (25) Wang, D. L. Threshold Lasing in Gallium Nitride Based Microcavities; Harvard University, 2019.

184798042096688.

- (26) Butler, T.P.; Goulding, D.; Kelleher, B.; O'Shaughnessy, B.; Slepneva, S.; Hegarty, S.P.; Huyet, G. Direct Experimental Measurement of Single-Mode and Mode-Hopping Dynamics in Frequency Swept Lasers. *Opt. Express* **2017**, *25* (22), 27464–27474.
- (27) Niu, N.; Woolf, A.; Wang, D.; Zhu, T.; Quan, Q.; Oliver, R. A.; Hu, E. L. Ultra-Low Threshold Gallium Nitride Photonic Crystal Nanobeam Laser. *Appl. Phys. Lett.* **2015**, *106* (23), 231104.
- (28) Netzel, C.; Hoffmann, V.; Tomm, J. W.; Mahler, F.; Einfeldt, S.; Weyers, M. Temperature-Dependent Charge Carrier Diffusion in [0001] Direction of GaN Determined by Luminescence Evaluation of Buried InGaN Quantum Wells. *Phys. status solidi* **2020**, 257 (6), 2000016.